The structural and electronic properties of nanostructured Ce$_{1-x-y}$Zr$_x$Tb$_y$O$_2$ ternary oxides: Unusual concentration of Tb^{3+} and metal↔oxygen↔metal interactions

Xianqin Wang, Jonathan C. Hanson, and José A. Rodriguez[a)]
Department of Chemistry, Brookhaven National Laboratory, Upton, New York 11973

Carolina Belver and Marcos Fernández-García[a)]
Instituto de Catálisis y Petroleoquímica, Consejo Superior de Investigaciones Científicas, (CSIC) Campus Cantoblanco, 28049 Madrid, Spain

Ceria-based ternary oxides are widely used in many areas of chemistry, physics, and materials science. Synchrotron-based time-resolved x-ray diffraction, x-ray absorption near-edge spectroscopy (XANES), Raman spectroscopy, and density-functional calculations were used to study the structural and electronic properties of Ce–Zr–Tb oxide nanoparticles. The nanoparticles were synthesized following a novel microemulsion method and had sizes in the range of 4–7 nm. The Ce$_{1-x-y}$Zr$_x$Tb$_y$O$_2$ ternary systems exhibit a complex behavior that *cannot* be predicted as a simple extrapolation of the properties of Ce$_{1-x}$Zr$_x$O$_2$, Ce$_{1-x}$Tb$_x$O$_2$, or the individual oxides (CeO$_2$, ZrO$_2$, and TbO$_2$). The doping of ceria with Zr and Tb induces a decrease in the unit cell, but there are large positive deviations with respect to the cell parameters predicted by Vegard's rule for ideal solid solutions. The presence of Zr and Tb generates strain in the ceria lattice through the creation of crystal imperfections and O vacancies. The O K-edge and Tb L_{III}-edge XANES spectra for the Ce$_{1-x-y}$Zr$_x$Tb$_y$O$_2$ nanoparticles point to the existence of distinctive electronic properties. In Ce$_{1-x-y}$Zr$_x$Tb$_y$O$_2$ there is an unexpected high concentration of Tb^{3+}, which is not seen in TbO$_2$ or Ce$_{1-x}$Tb$_x$O$_2$ and enhances the chemical reactivity of the ternary oxide. Tb↔O↔Zr interactions produce a stabilization of the Tb($4f$, $5d$) states that is responsible for the high concentration of Tb^{3+} cations. The behavior of Ce$_{1-x-y}$Zr$_x$Tb$_y$O$_2$ illustrates how important can be metal↔oxygen↔metal interactions for determining the structural, electronic, and chemical properties of a ternary oxide. © *2005 American Institute of Physics.* [DOI: 10.1063/1.1883631]

I. INTRODUCTION

The ability of ceria (CeO$_2$) to undergo a switch between "Ce^{4+}" and "Ce^{3+}" oxidation states has made this oxide a key component in the three-way catalysts (TWCs) commonly used to reduce the emissions of CO, NO$_x$, and hydrocarbons from automobile exhaust.[1] Ceria-supported noble-metal catalysts are capable of storing oxygen under oxidizing conditions or releasing oxygen under reducing conditions through a facile Ce^{4+}↔Ce^{3+} transformation.[1] In addition, CeO$_2$ has other important applications in many areas of chemistry, materials science, and physics.[1–3] It is a key component of solid-state electrochemical devices, which are used in fuel cells, chemical processing, and sensors.[1,3] In its most stable phase, bulk CeO$_2$ adopts a fluorite-type crystal structure in which each metal cation is surrounded by eight oxygen atoms.[1,4] The band gap of pure ceria is ~5 eV,[2,5] but crystal defects or impurities can transform the material into a good semiconductor.[1] Experimental and theoretical studies indicate that bulk CeO$_2$ is not a fully ionic oxide,[6–8] and is best described as an ionocovalent compound or covalent insulator.[6(c),8] The performance of ceria in automotive cata-

lysts, fuel cells, and electronic devices can be enhanced by doping this oxide with different types of metals (Zr, Ca, Cu, Tb, La, Mn, etc).[1,3(b),8–11] In general, this phenomenon is not fully understood. Of particular interest is to understand the behavior of mixed-metal oxides that contain Ce and other lanthanides.[1,8,10(c),10(d),11] Across the lanthanide series, there are significant variations in atomic size and electronegativity.[3(a),4]

How a given group of metals forms an oxide that has a specific set of properties is a fundamental question in solid-state chemistry and physics.[3(a),4,12,13] In the most simple approximation, one can assume that the properties of a mixed-metal oxide are an extrapolation of the properties of the single oxides (i.e., no metal↔oxygen↔metal interactions).[12,13] Thus, if one has a group of metals that forms single oxides with a particular crystal structure, then an ideal mixed-metal oxide should adopt this crystal structure and its lattice constant should be the sum of the lattice constants of the single oxides weighted by the composition of the system (Vegard's rule).[3(a),4,12,13] A vast number of alloys of metals and semiconductors obey Vegard's rule.[3(a),4,13] However, the behavior of a mixed-metal oxide may be non-ideal or unique as a consequence of structural and electronic perturbations introduced by metal↔oxygen↔metal interactions.[12–16] It is important to identify these structural

[a)]Authors to whom correspondence should be addressed. Electronic mail: rodrigez@bnl.gov; mfg@icp.csic.es

and electronic perturbations because they can determine the chemical reactivity of ceria-based oxides.[8,16,17]

In previous studies, we have examined the properties of $Ce_{1-x}Zr_xO_2$,[17,18] $Ce_{1-x}Ca_xO_2$,[19] and $Ce_{1-x}Tb_xO_2$.[8] In these oxide systems, cerium is mixed with a transition metal (Zr), an alkaline-earth metal (Ca), or a lanthanide (Tb). It is known that doping with Zr, Ca, and Tb affects the performance of ceria in catalytic processes.[1,10(a),20,21] We found that Zr mixing ($Ce_{1-x}Zr_xO_2$) improved the thermal stability of ceria nanoparticles, but did not introduce a significant number of oxygen vacancies.[17,18] On the other hand, Ca mixing ($Ce_{1-x}Ca_xO_2$) introduced a lot of oxygen vacancies in the host structure, but the mixed-metal oxide had a relatively low stability and phase segregation into CeO_2 and CaO was observed at temperatures close to 700 °C.[19] The Tb-containing oxides ($Ce_{1-x}Tb_xO_2$) displayed stability at high temperature against phase segregation and a reasonable concentration of O vacancies, being attractive for chemical and catalytic applications.[8] Ternary oxides are not uncommon in catalysis and materials science,[1,10(c),10(d),13] and there is a need to obtain a basic understanding of their behavior.[3(a),4,13,15] In this article, we investigate the structural and electronic properties of Ce–Zr–Tb oxide nanoparticles using x-ray absorption near-edge spectroscopy (XANES), Raman spectroscopy (RS), time-resolved x-ray diffraction (TR-XRD), and first-principles density-functional (DF) calculations. Our results clearly show that a ternary oxide can have distinctive electronic properties not seen for single or binary oxides. The behavior of $Ce_{1-x}Zr_xTb_yO_2$ *cannot* be predicted as a simple extrapolation of the behaviors of $Ce_{1-x}Zr_xO_2$ and $Ce_{1-x}Tb_xO_2$. In $Ce_{1-x-y}Zr_xTb_yO_2$, an unexpected very high concentration of Tb^{3+} and O vacancies is seen as a result of metal$\leftrightarrow$oxygen$\leftrightarrow$metal interactions. At a structural level, the lattice constants of the ternary oxide deviate significantly from values obtained using Vegard's rule.

II. EXPERIMENTAL AND THEORETICAL METHODS

A. Preparation of the Ce–Zr–Tb oxides

Oxide nanoparticles containing Ce, Zr, and Tb were prepared using an adaptation of the microemulsion method used previously for the synthesis of $Ce_{1-x}Zr_xO_2$ and $Ce_{1-x}Tb_xO_2$.[8,9,18] One of the samples contained equal amounts of the three cations, $Ce_{0.33}Zr_{0.33}Tb_{0.33}O_2$ (CZT111 in our notation). We also examined samples that had equal amounts of Ce and Zr, $Ce_{0.45}Zr_{0.45}Tb_{0.1}O_2$ and $Ce_{0.4}Zr_{0.4}Tb_{0.2}O_2$ (CZT992 and CZT442 in our notation), or equal amounts of Ce and Tb, $Ce_{0.45}Zr_{0.1}Tb_{0.45}O_2$ and $Ce_{0.4}Zr_{0.2}Tb_{0.4}O_2$ (CZT929 and CZT424 in our notation). In these systems, there are oxygen vacancies present (i.e., oxygen/metal ratio <2), but for simplicity we will label and refer to them as $Ce_{1-x-y}Zr_xTb_yO_2$.

B. Time-resolved XRD experiments

The time-resolved x-ray diffraction data were collected at beamlines X7B ($\lambda=0.922$ Å) and X17B1 ($\lambda=0.1655$ Å) of the National Synchrotron Light Source (NSLS) in Brookhaven National Laboratory (BNL). An identical setup

system was employed in both beamlines.[8,19,22] In the experiments dealing with the thermal stability and sintering of the $Ce_{1-x-y}Zr_xTb_yO_2$ nanoparticles, the sample was kept in a sapphire capillary and heated using a small resistance heater placed around the capillary.[22] A chromel–alumel thermocouple was used to measure the temperature of the sample. Two-dimensional powder patterns were collected with a Mar345 image plate detector and the powder rings were integrated using the FIT2D code.[23] From the high-energy XRD data, lattice constants were determined by a Rietveld analysis using the general structure analysis system (GSAS) program.[24] To calculate the strain in the lattice of the $Ce_{1-x-y}Zr_xTb_yO_2$ samples from the *in situ* data, we used the commercial REFLEX package[25] provided by Accelrys. The instrument parameters were derived from the fit of a Si reference pattern to the Thompson–Cox–Hastings profile coefficients[25(b)] and Baldinozzi–Berar asymmetry correction.[25(c)] Then, the sample size[25(d)] and strain[25(e)] were determined from the peak broadening in the nanoparticles. The cell dimensions determined by the methodologies mentioned above differed slightly (<0.04 Å) because different corrections were applied and different ranges of diffraction were used. The trends were identical and we have consistently used the cell parameters from the REFLEX package.
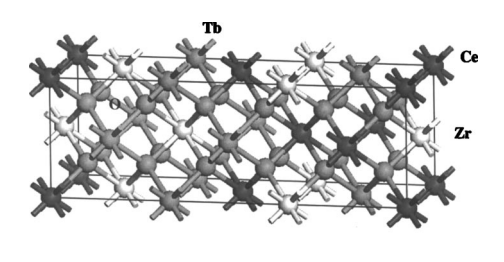
C. XANES experiments

The L_{III}-edge XANES spectra of Ce, Zr, and Tb were collected at the NSLS on beamline X19A in the "fluorescence-yield mode" using a boomerang-type flat crystal monochromator and a special cell with a modified Stern–Heald–Lytle detector.[8,18] Beamline U7A was utilized to record the O *K*-edge spectra. This beamline is equipped with a toroidal-spherical grating monochromator. The O *K*-edge spectra were taken in the "electron-yield mode" by using a channeltron multiplier located near the sample surface.[8,18] All the XANES spectra were taken at room temperature and the energy resolution was close to 0.5 eV.

D. Raman experiments

Raman spectra were obtained at room temperature with a Renishaw dispersive system 1000, equipped with a cooled thermal-conductivity detector (TCD) and holographic notch filter. The samples were excited with the 633 nm He:Ne laser line and the spectra consisted of 50 accumulations with a total of 10–15-min acquisition time, using a typical running power of 2–10 mW. Care was taken in minimizing heating of the samples; peak positions were seen constant within 2–3 cm^{-1}.

E. Theoretical methods

The first-principles DF calculations reported in Sec. III were performed using the Cambridge serial total-energy package (CASTEP) suite of programs.[26] CASTEP has an excellent track record in accurate prediction of geometry and energetics for oxide systems.[8,18,19,26(a),27] In this code, the wave functions of valence electrons are expanded in a plane-wave basis set with *k* vectors within a specified energy cutoff E_{cut}. Tightly bound core electrons are represented by

FIG. 1. Unit cell used to study the properties of bulk Ce$_{0.33}$Zr$_{0.33}$Tb$_{0.33}$O$_2$. The unit cell contains 4 atoms of Ce, 4 atoms of Zr, 4 atoms of Tb, and 24 atoms of O. The positions of the metal cations were exchanged in the unit cell to reflect a random solid solution (see text). In the figure is shown a possible configuration for the ternary oxide.

nonlocal ultrasoft pseudopotentials.[28] Brillouin-zone integration is approximated by a sum over special k points chosen using the Monkhorst–Pack scheme.[29] In all the calculations, the kinetic-energy cutoff E_{cut} (400 eV) and the density of the Monkhorst–Pack k-point mesh were chosen high enough in order to ensure convergence of the computed structures and energetics. The exchange-correlation contribution to the total electronic energy was treated in a generalized-gradient approximation (GGA) corrected form of the local-density approximation (LDA): Perdew–Burke–Ernzerhoff functional.[30]

To investigate the properties of the bulk Ce$_{0.33}$Zr$_{0.33}$Tb$_{0.33}$O$_2$ oxide, we employed the cell shown in Fig. 1, which contained 24 O atoms plus 4 atoms of Ce, Zr, and Tb (12 metal atoms in total). In a first approximation, the atoms of Zr and Tb were set in the pattern shown in Fig. 1. Then, possible permutations for the four Zr and four Tb atoms were considered, and the properties of Ce$_{0.33}$Zr$_{0.33}$Tb$_{0.33}$O$_2$ were determined by taking an average over all these permutations.[31] For each one of these permutations, we relaxed the crystal geometry before obtaining average values of lattice constants, metal-oxygen distances, charges, etc. The structural parameters of bulk CeO$_2$ and the Ce$_{0.33}$Zr$_{0.33}$Tb$_{0.33}$O$_2$ system in its different configurations were determined using the Broyden–Fletcher–Goldfarb–Shanno (BFGS) minimization technique, with the following thresholds for the converged structures: energy change per atom less than 5×10^{-6} eV, residual force less than 0.02 eV/Å, the displacement of atoms during the geometry optimization less than 0.001 Å, and the rms of the stress tensor less than 0.1 GPa.

For each optimized structure, the partial charges on the atoms were estimated by projecting the occupied one-electron eigenstates onto a localized basis set (which included pseudo-orbitals representing the valence levels of O, Ce, Zr, and Tb) with a subsequent Mulliken population analysis.[32] Any charge partition scheme has approximations,[33] but the Mulliken analysis has shown frequently to be useful for studying qualitative trends in charge distribution.[8,18,19]

III. RESULTS AND DISCUSSION

A. Structural properties of Ce$_{1-x-y}$Zr$_x$Tb$_y$O$_2$

For bulk CeO$_2$, the most stable conformation involves a fluorite-type structure in which each Ce atom is surrounded
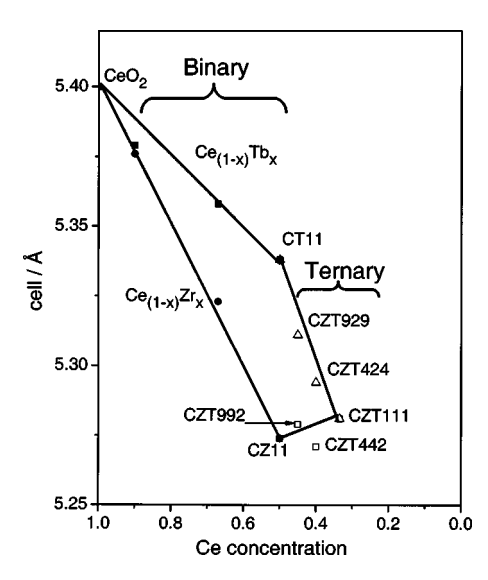

FIG. 2. Lattice constants determined by x-ray diffraction at 25 °C for nanoparticles of CeO$_2$, Ce$_{1-x}$Tb$_x$O$_2$, Ce$_{1-x}$Zr$_x$O$_2$, and Ce$_{1-x-y}$Zr$_x$Tb$_y$O$_2$. The notation used to label the mixed-metal oxides is explained in Sec. II A.

by eight oxygen atoms and the Ce–O bond distances are ~2.36 Å.[4] The corresponding lattice constant (a) is 5.41 Å. Figure 2 shows lattice constants determined by x-ray diffraction at room temperature for nanoparticles of CeO$_2$, Ce$_{0.5}$Tb$_{0.5}$O$_2$, Ce$_{0.5}$Zr$_{0.5}$O$_2$, Ce$_{0.33}$Zr$_{0.33}$Tb$_{0.33}$O$_2$, and several other Ce$_{1-x-y}$Zr$_x$Tb$_y$O$_2$ oxides. Transmission electron microscopy (TEM) images indicate that the nanoparticles have sizes ranging from 5 to 7 nm.[9] The small size of these systems limits the resolution of our structural analysis for the nanoparticles, and the a parameter listed in some cases may represent an average value for a pseudocubic phase with a slight tetragonal or related distortions. The results of DF calculations for bulk Ce$_{0.33}$Zr$_{0.33}$Tb$_{0.33}$O$_2$ and Raman spectra for the nanoparticles suggest the existence of small tetragonal-like distortions. In XRD, one would not expect to observe these slight tetragonal distortions because the diffraction peaks for the nanoparticles were very broad (see below).

A comparison of the cell parameters for CeO$_2$ (5.41 Å),[4] TbO$_2$ (5.22 Å),[34] and cubic ZrO$_2$ (5.15 Å)[4,17] indicates that Tb^{4+} is smaller than Ce^{4+} and larger than Zr^{4+}. In Fig. 2, one can see a clear decrease in the lattice constant of the oxide after mixing Ce with Tb or Zr. The largest cell reduction is observed for the Zr-containing oxides. When going from Ce$_{0.5}$Tb$_{0.5}$O$_2$ (CT11) to Ce$_{0.33}$Zr$_{0.33}$Tb$_{0.33}$O$_2$ (CZT111), the Ce/Tb ratio is maintained equal but the amount of Zr in the oxide increases from 0% to 33%. The Ce↔Zr and Tb↔Zr substitutions induce a large reduction in the cell dimension, displaying a linear trend with a slope roughly similar to that characteristic of the Ce$_{(1-x)}$Zr$_x$ binary system. This would mean that Zr addition to CeO$_2$ or Ce$_{0.5}$Tb$_{0.5}$O$_2$ systems induces, to a first approximation, similar long-range structural effects. In the bottom branch, when going from Ce$_{0.5}$Zr$_{0.5}$O$_2$ (CZ11) to Ce$_{0.33}$Zr$_{0.33}$Tb$_{0.33}$O$_2$ (CZT111), the Ce/Zr ratio is kept equal while the amount of Tb in the oxide rises from 0% to 33%. The Zr↔Tb exchange leads to only a small increase in the cell dimensions. This fact is obviously at odds with the expected result coming from the application of the Vegard's
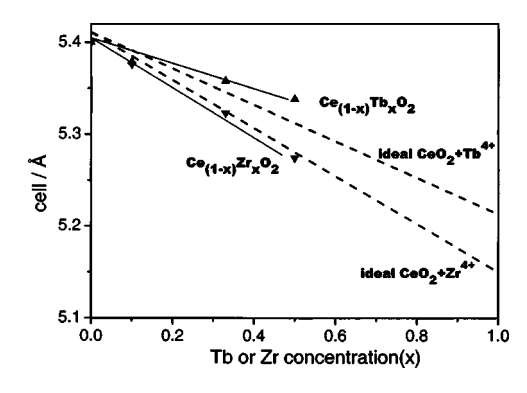
FIG. 3. Cell parameters determined for $Ce_{1-x}Zr_xO_2$ and $Ce_{1-x}Tb_xO_2$ nanoparticles from XRD patterns (solid lines) and estimated using Vegard's rule (Ref. 35) and the experimental lattice parameters for bulk CeO_2 (Ref. 4), TbO_2 (Ref. 34), and ZrO_2 (Refs. 4 and 17) (dashed lines).

rule. In these oxide systems, the relatively large concentration of Zr (50%–33%) seems to dominate and maintains the cell dimension small.

For bulk CeO_2, our DF calculations give a lattice constant of 5.46 Å. In the case of bulk $Ce_{0.33}Zr_{0.33}Tb_{0.33}O_2$, the DF calculations predict an average unit cell that is pseudocubic, with a small tetragonal-like distortion ($a = 5.27$ Å, $b = 5.28$ Å, and $c = 5.31$ Å). Thus, from the theoretical results one can expect a cell contraction of ~0.17 Å, which is significantly larger than the value of ~0.12 Å observed in Fig. 2 for the $Ce_{0.33}Zr_{0.33}Tb_{0.33}O_2$ sample. The difference between the theoretical and experimental values decreased as a result of introducing O vacancies in the model shown in Fig. 1. The results of a Rietveld analysis of the XRD patterns and XANES data to be presented in the next section indicate that there was a large concentration of O vacancies and Tb^{3+} in the $Ce_{1-x-y}Zr_xTb_yO_2$ nanoparticles. If one uses Vegard's rule[35] together with the DF calculated lattice constants for bulk CeO_2 (5.46 Å),[18] ZrO_2 (5.11 Å),[18] and TbO_2 (5.22 Å),[8] one gets a lattice constant of 5.26 Å for bulk $Ce_{0.33}Zr_{0.33}Tb_{0.33}O_2$. According to the DF calculations, the stoichiometric $Ce_{0.33}Zr_{0.33}Tb_{0.33}O_2$ oxide (average unit-cell parameter ~5.29 Å) shows a small positive deviation with respect to the prediction of the Vegard's rule. This issue can be examined in more detail using XRD data.

Figure 3 compares cell parameters determined for $Ce_{1-x}Zr_xO_2$ and $Ce_{1-x}Tb_xO_2$ nanoparticles from XRD patterns (solid lines) with cubiclike cell parameters estimated using Vegard's rule[35] and the experimental lattice parameters for bulk CeO_2,[4] TbO_2,[34] and ZrO_2[4,17] (dashed lines). The $Ce_{1-x}Zr_xO_2$ systems obey Vegard's rule, and a $Ce \leftrightarrow Zr$ exchange produces a monotonic decrease in the cell dimensions of the oxide. In contrast, the cell parameters for $Ce_{1-x}Tb_xO_2$ show a positive deviation from Vegard's rule. Something similar was observed in the density-functional calculations for bulk $Ce_{0.75}Tb_{0.25}O_2$ and $Ce_{0.5}Tb_{0.5}O_2$. The discrepancy is in part caused by the fact that in $Ce_{1-x}Tb_xO_2$, a substantial fraction of the terbium is present as Tb^{3+} instead of Tb^{4+} (see Sec. III B). In Tb_2O_3 the metal cations have a larger radii than in TbO_2, and the crystal structure is different from the fluorite type.[8,34]

Figure 4 compares cell parameters for $Ce_{1-x-y}Zr_xTb_yO_2$ nanoparticles obtained from XRD (solid line) and Vegard's
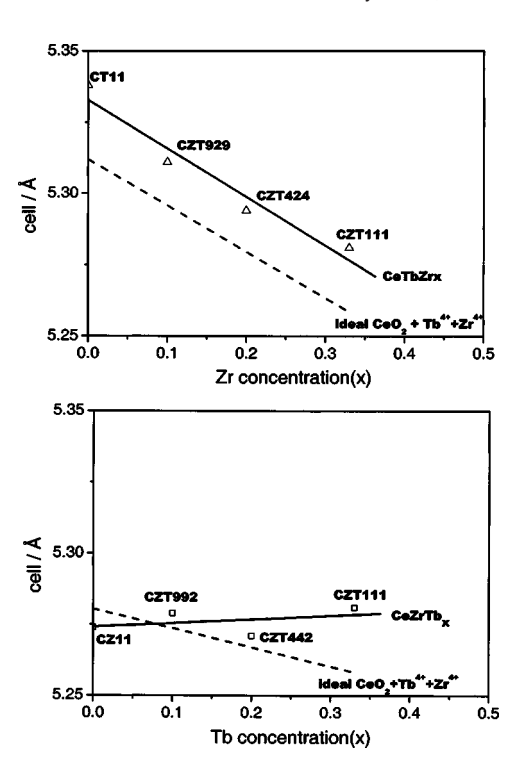

FIG. 4. Cell parameters for $Ce_{1-x-y}Zr_xTb_yO_2$ nanoparticles obtained from XRD (solid line) and Vegard's rule (dashed line). In the top panel, the Ce/Tb ratio is maintained constant while Zr is added. In the bottom panel, Tb is added keeping the Ce/Zr ratio constant.

rule (dashed line). In the top panel, we start with $Ce_{0.5}Tb_{0.5}O_2$ and Zr is introduced keeping the Ce/Tb ratio constant. Initially, the $Ce_{0.5}Tb_{0.5}O_2$ system deviates from the Vegard's rule, but upon the addition of Zr, there is a linear decrease in the cell dimensions as the Vegard's rule predicts. In the bottom panel of Fig. 4, the starting point is $Ce_{0.5}Tb_{0.5}O_2$ and Tb is added. In these ternary oxides, one sees a behavior for the cell parameters that is opposite to the expectations from Vegard's rule. As we will see below, the XANES spectra for these oxides show the dominant presence of Tb^{3+} and very little Tb^{4+} in addition to differences in Zr local order. In fact, for stoichiometric $Ce_{0.33}Zr_{0.33}Tb_{0.33}O_2$, the DF calculations predict a local structure around the cations that shifts the oxygens to positions different from those seen in the fluorite cells of CeO_2, ZrO_2, or TbO_2. These structural distortions, which contrast with the ideal predictions of the Vegard's rule, are a consequence of forcing the coexistence of Zr^{4+} and Tb^{4+} cations into an oxide lattice that is too big for their ionic radii.

From the variation of the peak width with 2θ in powder diffraction, one can obtain a strain parameter[25] that is a measure of the lattice stress existing in the oxide because of crystal imperfections:[16] O vacancies, other point defects, line defects, and plane defects. In previous studies, a qualitative correlation between the chemical reactivity and the strain parameter of ceria-based nanoparticles was found.[8,17] A strong correlation between oxygen storage capacity and lattice strain has been observed for $Ce_{1-x}Zr_xO_2$.[10(e)] Figure 5 shows the strain parameter obtained from XRD results for CeO_2, $Ce_{0.5}Zr_{0.5}O_2$, $Ce_{0.5}Tb_{0.5}O_2$, and $Ce_{1-x-y}Zr_xTb_yO_2$ nanoparticles. Pure ceria nanoparticles exhibit a lattice strain
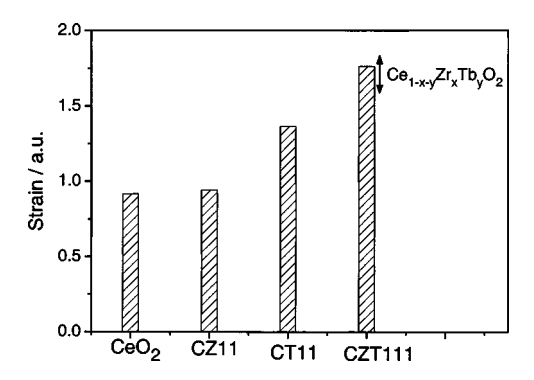
FIG. 5. Strain parameter (obtained from XRD patterns at 25 °C) for CeO$_2$, Ce$_{0.5}$Zr$_{0.5}$O$_2$, Ce$_{0.5}$Tb$_{0.5}$O$_2$, and Ce$_{1-x-y}$Zr$_x$Tb$_y$O$_2$ nanoparticles.

when compared to bulk CeO$_2$.[8,18] The introduction of an alien species such as Tb leads to extra forces that increase the strain in the lattice of the nanoparticles. But the amount of stress does not correlate linearly with the total terbium concentration, being larger for Ce$_{0.33}$Zr$_{0.33}$Tb$_{0.33}$O$_2$ than for Ce$_{0.5}$Tb$_{0.5}$O$_2$. Perhaps, one could expect more lattice imperfections in a ternary oxide than in a binary oxide. This would be consistent with a larger quantity of Tb^{3+} in the ternary oxides (see Sec. III B).

Raman spectroscopy can be useful to detect the oxygen sublattice distortions predicted by DF calculations and the existence of O vacancies in ceria-based materials.[16] Raman spectra taken at 25 °C for a series of Ce$_{1-x-y}$Zr$_x$Tb$_y$O$_2$ nanoparticles are shown in Fig. 6. As a general result, the spectra show three well-defined bands at ca. 604, 474–5, and 282 cm^{-1}, and maybe a broad contribution at the high wavenumber side of the 604 cm^{-1} peak. The Ce$_{1-x-y}$Zr$_x$Tb$_y$O$_2$ nanoparticles Raman spectra mainly differ in the behavior of this latter peak. While its height and width are rather constant for samples having a 1:1 Ce:Tb atomic ratio, both parameters are clearly sensible to the Tb quantity present in samples with a 1:1 Ce:Zr atomic ratio. This fact and the presence of a similar peak in the TbO$_{1.7}$ reference[8] would indicate a somewhat localized nature and/or dominant contribution of O ions near Tb in this peak, which may be thus indicative of a specific structural distortion around this cation in the ternary oxides. It should be, however, noted that UV-vis spectra (results not shown) indicate a gradual loss of absorbance at 633 nm for samples having a 1:1 Ce:Zr atomic ratio and decreasing quantities of Tb. Therefore, the sample
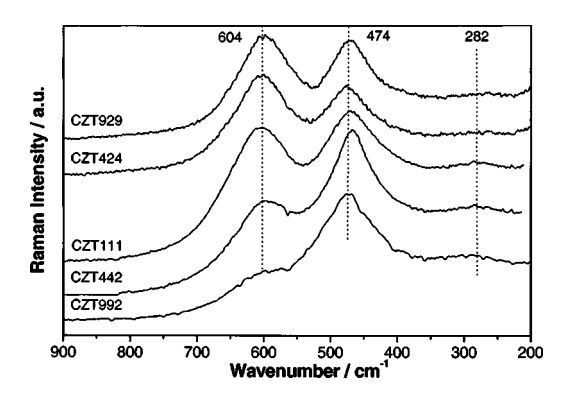

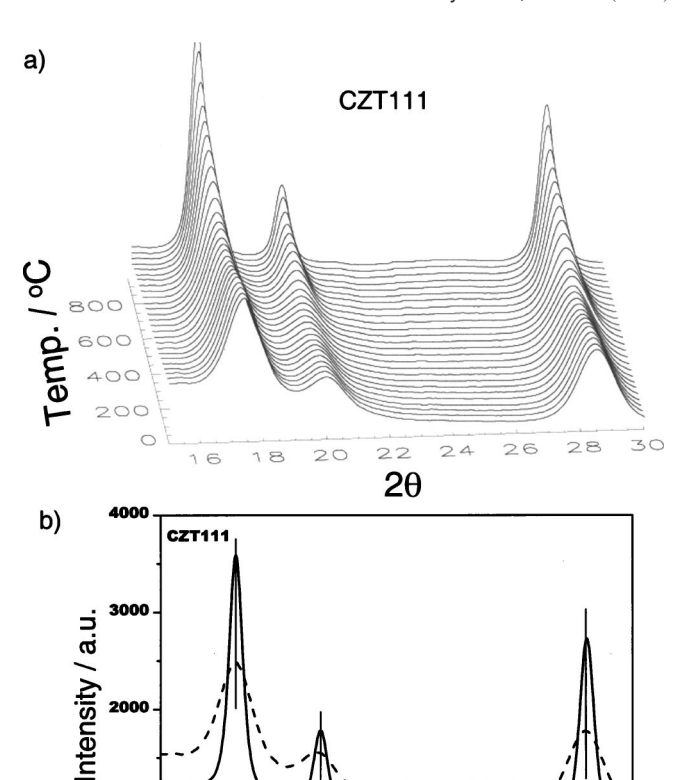FIG. 6. Raman spectra taken at 25 C for a series of Ce$_{1-x-y}$Zr$_x$Tb$_y$O$_2$ nanoparticles.

FIG. 7. Time-resolved XRD results obtained after heating a sample of Ce$_{0.33}$Zr$_{0.33}$Tb$_{0.33}$O$_2$ nanoparticles from 25 to 925 °C. Heating rate = 6 °C/min, and λ = 0.922 Å.

depth analyzed by Raman varies significantly and differences in Tb radial distribution in the nanoparticles may also affect the 604-cm^{-1} peak behavior. A nonhomogeneous radial distribution of Tb is, however, not expected due to the lack of segregation after treatment at high temperatures (see below). This phenomenon does not occur in the 1:1 Ce:Tb series as their absorbance at 633 nm is rather high in all cases.

Based on previous experience with Ce binary oxides,[8,18–21] the presence of two bands at ca. 600–550 and 250 cm^{-1} together with the F$_{2g}$ fluorite-related 475 cm^{-1} peak can be associated with simple structural distortions of the cubic-fluorite oxygen sublattice. The broad peak at 604 cm^{-1} may also content a vacancy-related second-order contribution.[36(b)] In any case, the spectra are compatible with a pseudocubic, tetragonal t'' symmetry,[36] and consistent with the tetragonal-like symmetry obtained from the DF calculations. The marked asymmetry of the main 475 cm^{-1} peak and the broad nature of all contributions with respect to a CeO$_2$ nanoparticle reference[8] indicate the existence of strong phonon confinement effects,[16] which could be a consequence of either a nonhomogeneous distribution of vacancy domains (ordering effect of the vacancy distribution) and/or the structural distortion of the oxygen sublattice already mentioned.

Figure 7 shows time-resolved XRD results obtained after heating a sample of Ce$_{0.33}$Zr$_{0.33}$Tb$_{0.33}$O$_2$ nanoparticles from 25 to 925 °C. At room temperature, the diffraction lines are broad due to the very small size of the particles (~4 nm).
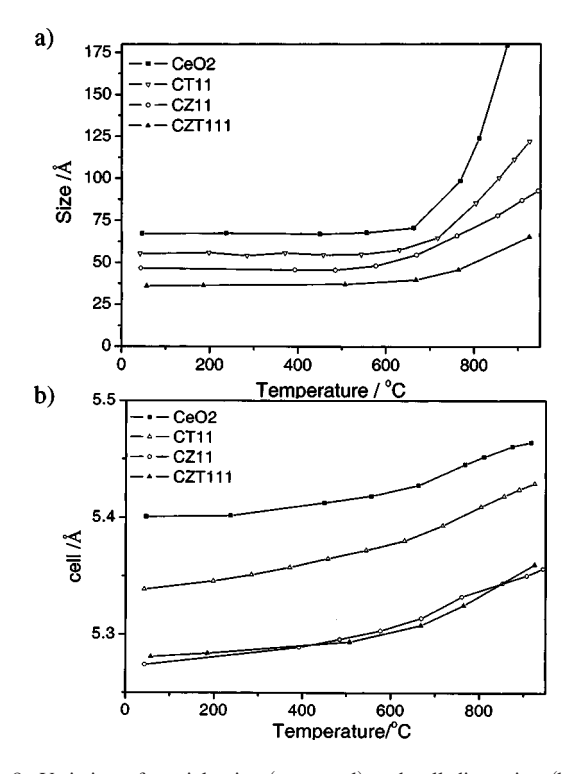
a)

b)

FIG. 8. Variation of particle size (top panel) and cell dimension (bottom panel) with temperature for nanoparticles of CeO_2, $Ce_{0.5}Zr_{0.5}O_2$ (CZ11), $Ce_{0.5}Tb_{0.5}O_2$ (CT11), and $Ce_{0.33}Zr_{0.33}Tb_{0.33}O_2$ (CZT111). Heating rate = 6 °C/min.

They match well with the diffraction pattern for a structure of the CeO_2 fluorite type.[4,8] Up to 550 °C, only minor changes in the diffraction lines are seen. Above 600 °C, the diffraction lines for the mixed-metal oxide become sharper and intense due to sintering of the nanoparticles. After the sintering, there is a small change in the relative position of the diffraction lines that points again to a slight cell distortion. This is consistent with the DF results for bulk $Ce_{0.33}Zr_{0.33}Tb_{0.33}O_2$. The results of time-resolved XRD displayed in Fig. 7 are typical of those found upon the heating of the $Ce_{1-x-y}Zr_xTb_yO_2$ nanoparticles. For all of these systems, there was no segregation of TbO_x or ZrO_x phases at elevated temperatures.

The top panel in Fig. 8 shows the effects of temperature on the particle sizes of nanoparticles of CeO_2, $Ce_{0.5}Zr_{0.5}O_2$, $Ce_{0.5}Tb_{0.5}O_2$, and $Ce_{0.33}Zr_{0.33}Tb_{0.33}O_2$. The particle sizes were refined from TR-XRD data using a whole profile method. In general, they agree with the sizes seen in TEM images taken at room temperature.[9] At temperatures above 600 °C, there is sintering and the particle size rises. The amount of sintering is smaller for the ternary $Ce_{0.33}Zr_{0.33}Tb_{0.33}O_2$ oxide. This is visible in the slopes of the linear behavior detected above 600 °C; these slopes decrease in the order $CeO_2 > Ce_{0.5}Tb_{0.5}O_2 > Ce_{0.5}Zr_{0.5}O_2 > Ce_{0.33}Zr_{0.33}Tb_{0.33}O_2$. The bottom panel in Fig. 8 displays the effects of temperature on the cell dimensions of the oxide nanoparticles. Two different slopes are observed with the break point at around 600 °C. The different slopes imply that the change in cell dimension was not only a consequence of thermal expansion, which dominates below 600 °C,[8] but was also affected by the sintering process above that point.

TABLE I. Calculated Mulliken charges (e)

Compound	q(Ce)	q(Zr)	q(Tb)
CeO_2	1.42	⋯	⋯
$Ce_{0.5}Zr_{0.5}O_2$	1.57	1.39	⋯
$Ce_{0.5}Tb_{0.5}O_2$	1.48	⋯	1.47
$Ce_{0.33}Zr_{0.33}Tb_{0.33}O_2$	1.52	1.35	1.45

B. Electronic properties of $Ce_{1-x-y}Zr_xTb_yO_2$

Experimental and theoretical studies indicate that bulk CeO_2 is not a fully ionic oxide,[6–8] and is best described as an ionocovalent compound or covalent insulator.[6(c),8] The results of the DF calculations for bulk $Ce_{0.33}Zr_{0.33}Tb_{0.33}O_2$ indicate that the charges on the cations are far from the formal value of +4. The valence bands of the oxide contain not only O $2p$ character but also a significant contribution from orbitals of Ce, Zr, and Tb. Table I compares Mulliken charges calculated for bulk CeO_2, $Ce_{0.5}Zr_{0.5}O_2$, $Ce_{0.5}Tb_{0.5}O_2$, and $Ce_{0.33}Zr_{0.33}Tb_{0.33}O_2$. The Ce↔Zr and Ce↔Tb substitutions produce an increase in the positive charge of the Ce atoms that remain in the oxide lattice. In the ternary oxide, there is an important contraction of the cell parameters (~0.12 Å) with respect to CeO_2 that leads to a reduction in the Ce–O bond distances and, thus,[18] should give an increase in the positive charge of cerium. Metal↔oxygen↔metal interactions[15,19,31] also contribute to enhance the Ce positive charge.

Figure 9 displays O K-edge XANES spectra taken at room temperature for CeO_2 and the $Ce_{1-x-y}Zr_xTb_yO_2$ nano-
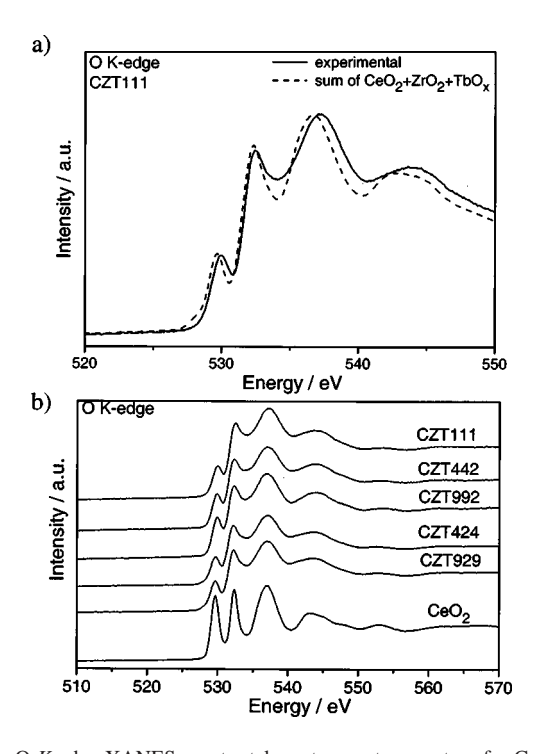
a)

b)

FIG. 9. O K-edge XANES spectra taken at room temperature for CeO_2 and $Ce_{1-x-y}Zr_xTb_yO_2$ nanoparticles. The notation used to label the mixed-metal oxides is explained in Sec. II A. The top panel compares the experimental spectrum (solid trace) for $Ce_{0.33}Zr_{0.33}Tb_{0.33}O_2$ nanoparticles and that obtained by adding the corresponding spectra for CeO_2, ZrO_2 (Ref. 18), and TbO_x (Ref. 8) weighted by the concentration of the metals in the ternary oxide (dashed line).
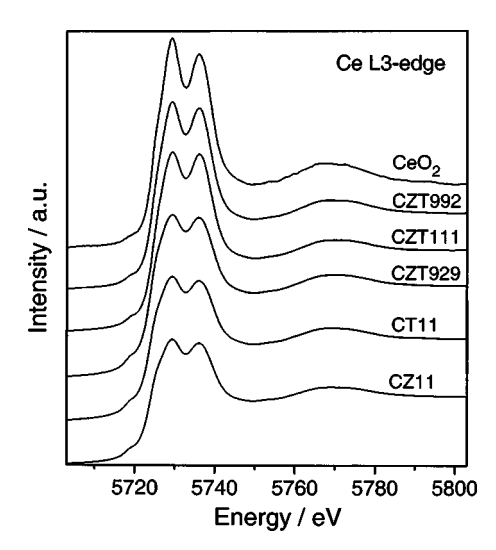
FIG. 10. Ce L_{III}-edge XANES spectra for CeO$_2$ and Ce$_{1-x-y}$Zr$_x$Tb$_y$O$_2$ nanoparticles taken at room temperature.

FIG. 11. Room-temperature Zr L_{III}-edge XANES spectra for monoclinic ZrO$_2$, Ce$_{0.5}$Zr$_{0.5}$O$_2$, and Ce$_{1-x-y}$Zr$_x$Tb$_y$O$_2$ nanoparticles.

particles. The first three peaks in the spectrum for pure CeO$_2$ are related to electronic transitions from the O 1s core levels into the empty O 2p-hole states located in the cerium-dominated 4f, 5de_g, and 5dt_{2g} levels/bands.[18] Once that zirconium and terbium are present in the oxide, then electronic transitions from the O 1s core levels to the O 2p-hole states located in Zr(4d)- and Tb(4f,5d)-dominated states are possible.[8,18] The addition of Zr and Tb to ceria produces substantial changes in the line shape of the O K-edge region. The top panel in Fig. 9 compares the experimental spectrum (solid trace) for Ce$_{0.33}$Zr$_{0.33}$Tb$_{0.33}$O$_2$ nanoparticles and that obtained by adding the corresponding spectra for CeO$_2$, ZrO$_2$,[18] and TbO$_x$ (Ref. 8) weighted by the concentration of the metals in the ternary oxide (dashed line). There are small but clear differences in the line shape of the experimental and calculated spectra. This can be detected in the energy position of the four Ce-dominated continuum resonances (CRs) visible in the spectra; they are shifted from the "sum" spectrum maxima according to the (E_R-E_0) R^2=const rule (where E_R is the energy of the resonance, E_0 is the zero of the photoelectron kinetic energy, and R is the first coordination distance)[37] which predicts a larger separation for CRs located at higher energy, indicating that the main difference between these two spectra is related to the cell parameter contraction of the ternary system with respect to the CeO$_2$ reference system. Besides this, the peaks are broadened by the increasing disorder of the ternary oxide (see strain discussion in Sec. III A) as well as by the presence of the mentioned Zr and Tb contributions.

Ce L_{III}-edge XANES spectra for CeO$_2$ and Ce$_{1-x-y}$Zr$_x$Tb$_y$O$_2$ nanoparticles are shown in Fig. 10. The Ce L_{III} edge is frequently used as a "fingerprint" to characterize the electronic properties of ceria-based materials.[16,18,37,38] However, the electronic transitions behind these XANES features are complex and not fully understood.[37,38] The two main peaks correspond to two final-state configurations, describable as [*]4f^1L^{n-1}5d^1 and [*]4f^0L^n5d^1.[38] The Ce L_{III}-edge spectra for the mixed-metal oxides show minor dif-
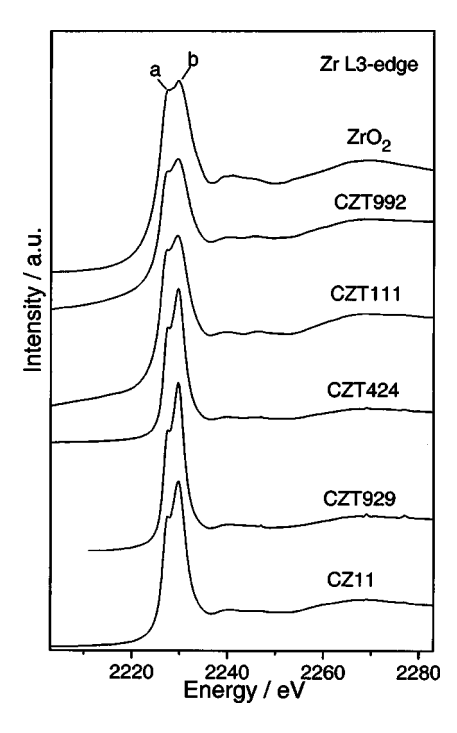
ferences with respect to that for pure CeO$_2$. No clear signal is seen for the presence of cerium atoms in a formal oxidation state of "+3".[16,19,37,38]

Figure 11 displays Zr L_{III}-edge spectra for bulk ZrO$_2$ and Ce$_{1-x-y}$Zr$_x$Tb$_y$O$_2$ nanoparticles. At the temperatures at which the spectra were acquired (~25 °C), a monoclinic crystal structure is the thermodynamically stable phase for microsized or bulk ZrO$_2$.[4,16] The two main features (a,b) in the Zr L_{III} edge correspond to electronic transitions from the occupied Zr 2p orbitals to the empty Zr 4d orbitals, which are split into orbitals with t and e symmetry.[37,39] In oxides, the relative intensity of the a and b peaks depends strongly on the chemical environment around the Zr cations.[18,39] For the Ce$_{0.5}$Zr$_{0.5}$O$_2$, Ce$_{0.45}$Zr$_{0.1}$Tb$_{0.45}$O$_2$, and Ce$_{0.40}$Zr$_{0.2}$Tb$_{0.40}$O$_2$ nanoparticles, the Zr atoms seem to have a local geometry that is different from that of monoclinic ZrO$_2$ or tetragonal Zr doped into Y$_2$O$_3$.[39] In fact, this result indicates a pseudocubic, tetragonal t'' structure similar to that of the Ce$_{0.5}$Zr$_{0.5}$O$_2$ reference, and thus a 4+2 oxygen coordination.[40] On the other hand, for Ce$_{0.33}$Zr$_{0.33}$Tb$_{0.33}$O$_2$ and Ce$_{0.45}$Zr$_{0.45}$Tb$_{0.1}$O$_2$, the line shape of the Zr L_{III}-edge spectra indicates that the Zr atoms have a local geometry similar to that of monoclinic ZrO$_2$ and a 4+3 oxygen first shell coordination.[40] This can help to explain why the cell parameters of these systems deviate so much from the predictions of Vegard's rule (bottom panel in Fig. 4). A point to remark is that the presence of Tb in ternary systems having equal amounts of Ce and Zr strongly influences the local geometry of Zr, modifying the typical one characteristic of the "parent" Ce$_{0.5}$Zr$_{0.5}$O$_2$ binary system.[9,10,18] Independently of the local geometry, Zr is in the +4 oxidation state through the ternary series studied.

Tb L_{III}-edge spectra for a TbO$_x$ reference (probably Tb$_4$O$_7$,[41] stoichiometric TbO$_2$ is very difficult to prepare[34])
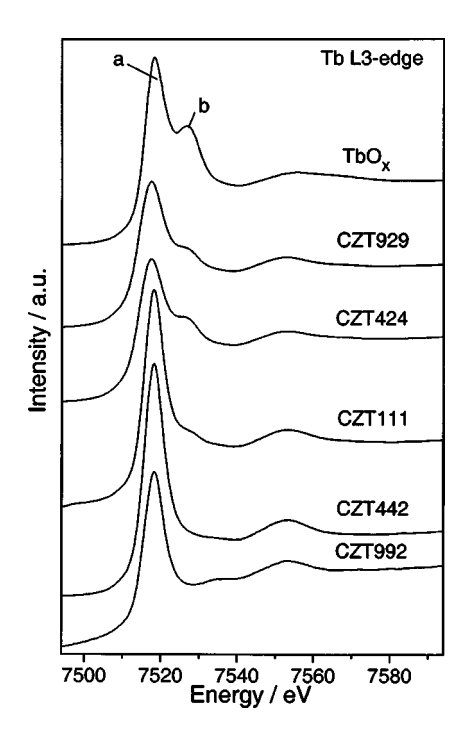
FIG. 12. Tb L_{III}-edge spectra for a TbO_x reference (probably Tb_4O_7) and $Ce_{1-x-y}Zr_xTb_yO_2$ nanoparticles at 25 °C.

and $Ce_{1-x-y}Zr_xTb_yO_2$ nanoparticles are compared in Fig. 12. Two intense components, *a* and *b*, and a weak, broad one are evident in the spectrum for TbO_x. In terbium oxides, the *a*/*b* intensity ratio increases when Tb^{4+} is progressively reduced to Tb^{3+}.[8,37,42] All lanthanide oxides only display a single peak near the edge (white line) for the +3 state.[37,42] The XANES spectra in Fig. 12 indicate that $Ce_{0.45}Zr_{0.45}Tb_{0.1}O_2$ and $Ce_{0.4}Zr_{0.4}Tb_{0.2}O_2$ only contain Tb^{3+}, a trace of Tb^{4+} may be present in $Ce_{0.33}Zr_{0.33}Tb_{0.33}O_2$, with a small amount of Tb^{4+} in $Ce_{0.4}Zr_{0.2}Tb_{0.4}O_2$ and $Ce_{0.45}Zr_{0.1}Tb_{0.45}O_2$. This trend in the content of Tb^{3+} agrees with the trend found for the O occupancies in a Rietveld analysis of the corresponding XRD patterns. The high concentration of Tb^{3+} in the ternary oxides is unexpected. If one compares to TbO_x and $Ce_{1-x}Tb_xO_2$ samples,[8] one finds that the $Ce_{1-x-y}Zr_xTb_yO_2$ compounds always have a relatively low content of Tb^{4+}, even when the concentration of terbium is as high as 33%. In order to understand this phenomenon better, we used DF calculations to examine the formation of oxygen vacancies in bulk CeO_2, TbO_2, $Ce_{0.66}Tb_{0.33}O_2$, and $Ce_{0.33}Zr_{0.33}Tb_{0.33}O_2$.

Starting with the unit cell shown in Fig. 1, we calculated the ΔE associated with the following reactions:

$$Ce_{12}O_{24}(solid) \rightarrow Ce_{12}O_{22}(solid) + O_2(gas), \qquad (1)$$

$$Tb_{12}O_{24}(solid) \rightarrow Tb_{12}O_{22}(solid) + O_2(gas), \qquad (2)$$

$$Ce_8Tb_4O_{24}(solid) \rightarrow Ce_8Tb_4O_{22}(solid) + O_2(gas), \qquad (3)$$

$$Ce_4Zr_4Tb_4O_{24}(solid) \rightarrow Ce_4Zr_4Tb_4O_{22}(solid) + O_2(gas). \qquad (4)$$

In principle, if one assumes the validity of formal oxidation states, the removal of two O atoms from the unit cell leaves behind four electrons that can be used to reduce the charge of four metal cations from +4 to +3. Of course, the process is more complex than this because none of the oxides in reactions (1)–(4) is fully ionic. The results of the DF calculations indicate that the energy necessary for the removal of O decreases following the sequence: $Ce_{12}O_{24} > Tb_{12}O_{24} > Ce_8Tb_4O_{24} > Ce_4Zr_4Tb_4O_{24}$. For pure ceria reaction (1) is highly endothermic,[1,19] while for the ternary oxide reaction (4) is slightly exothermic ($\Delta E = -0.12$ eV per cell, or -0.005 eV per O atom). In the reduced $Ce_8Tb_4O_{22}$ and $Ce_4Zr_4Tb_4O_{22}$ systems, the most stable configurations were those in which the O vacancies were close to Tb atoms. In these mixed-metal oxides, the electrons left behind after the removal of O go to empty bands mainly dominated by Tb($4f, 5d$) character. In practical terms only the Tb is reduced. The empty bands with Tb($4f, 5d$) character are more stable in the mixed-metal oxides than in the pure terbium oxide. The causes for this phenomenon are in metal↔oxygen↔metal interactions and in the fact that Tb is located in oxide cells which are larger than that of TbO_2. Thus, there is a reduction in electron–electron repulsion and the extra volume necessary for a $Tb^{4+} \rightarrow Tb^{3+}$ reduction is more available in the mixed-metal oxides. These effects are particularly important in the $Ce_{0.33}Zr_{0.33}Tb_{0.33}O_2$ system, where there are significant Tb↔O↔Zr interactions and the volume occupied by the Zr cations in the oxide lattice is smaller than those of the Ce or Tb cations. The net result is a stabilization of the Tb($4f, 5d$) states and a very large concentration of Tb^{3+} cations.

C. Tb^{3+} concentration, lattice defects, and the chemical activity of $Ce_{1-x-y}Zr_xTb_yO_2$ nanoparticles

The magnitude of the strain parameter in Fig. 5 correlates with the amount of oxygen vacancies in the oxide nanoparticles. XANES shows the absence of Ce^{3+} in all of the samples, and there is no Zr^{3+} in the $Ce_{0.5}Zr_{0.5}O_2$ or $Ce_{1-x-y}Zr_xTb_yO_2$ systems. In contrast, Tb^{3+} is present in the $Ce_{0.5}Tb_{0.5}O_2$ (Ref. 8) and $Ce_{1-x-y}Zr_xTb_yO_2$ systems, being by far the dominant terbium species in the ternary oxides. The stoichiometry of our ternary mixed oxides is thus rather close to $Ce_{1-x-y}Zr_xTb_yO_{2-y/2}$. It must be pointed out that not only O vacancies contribute to the strain parameter other point defects, line defects, and plane defects are important.[16] All of these have an effect in the average size of the unit cell and, thus, contribute to the deviations seen in Figs. 3 and 4 with respect to the Vegard's rule predictions. The ternary systems are clearly nonideal, and one cannot predict their behavior as an extrapolation of the behavior observed for the single oxides or the Ce–Zr and Ce–Tb binary mixtures. The Ce↔Zr and Ce↔Tb exchanges introduce metal↔oxygen↔metal interactions that are unique for the ternary oxide.

In previous studies a qualitative correlation between the strain parameter and the chemical reactivity of oxide nanoparticles was found.[8,10(e),17] Studies with well-defined single-crystal surfaces have shown the important role that O vacancies and structural imperfections play in the chemical properties of ceria-based oxides.[17,43] The reduction by reaction with H_2 and the cleavage of the S–O bonds in adsorbed SO_2 should be affected by the high concentration of Tb^{3+}

cations and lattice defects in the $Ce_{1-x-y}Zr_xTb_yO_2$ nanoparticles.[8,17] Indeed, preliminary studies of H_2-temperature programmed reduction indicate that these ternary oxides start to react with H_2 (50–100 °C) much sooner than pure ceria nanoparticles (>300 °C).[44] In addition, the adsorption of SO_2 on ceria nanoparticles at 25 °C produces SO_4/SO_3 groups with a negligible decomposition of the adsorbate,[17] whereas on $Ce_{0.33}Zr_{0.33}Tb_{0.33}O_2$ a substantial amount of sulfur is deposited on the oxide as a result of S–O bond cleavage.[44]

$Ce_{1-x}Tb_xO_2$ compounds have been reported to have a superior performance in the storage or release of oxygen when forming part of the three-way catalysts (TWC) used to reduce the emissions of CO, NO_x, and hydrocarbons from automobile exhaust.[20,21,45] It was proposed that the presence of O vacancies associated with Tb^{3+} contributed to enhance the oxygen mobility.[21] In this respect, since the concentration of Tb^{3+} in $Ce_{1-x-y}Zr_xTb_yO_2$ is larger than in $Ce_{1-x}Tb_xO_2$, one can expect that the ternary oxides will be very good for the storage/release of oxygen.

IV. SUMMARY AND CONCLUSIONS

Synchrotron-based time-resolved XRD, XANES, Raman spectroscopy, and first-principles DF calculations were used to study the structural and electronic properties of Ce–Zr–Tb oxide nanoparticles. The $Ce_{1-x-y}Zr_xTb_yO_2$ ternary systems exhibit a complex behavior that cannot be predicted as a simple extrapolation of the properties of $Ce_{1-x}Zr_xO_2$, $Ce_{1-x}Tb_xO_2$, or the individual oxides (CeO_2, ZrO_2, and TbO_2). The doping of ceria with Zr and Tb induces a decrease in the oxide unit cell, but there are large positive deviations with respect to the cell parameters predicted by Vegard's rule for ideal solid solutions. The presence of Zr and Tb generates strain in the fluorite lattice through the creation of crystal imperfections and O vacancies.

The $Ce_{1-x-y}Zr_xTb_yO_2$ systems are not fully ionic, and are best described as ionocovalent compounds. The valence bands of the ternary oxides contain not only O $2p$ character but also a significant contribution from orbitals of Ce, Zr, and Tb. The O K-edge and Tb L_{III}-edge XANES spectra for the $Ce_{1-x-y}Zr_xTb_yO_2$ nanoparticles point to the existence of distinctive electronic properties. In $Ce_{1-x-y}Zr_xTb_yO_2$ there is an unexpected high concentration of Tb^{3+}, which is not seen in TbO_2 or $Ce_{1-x}Tb_xO_2$ and enhances the chemical reactivity of the ternary oxide. $Tb \leftrightarrow O \leftrightarrow Zr$ interactions produce a stabilization of the $Tb(4f, 5d)$ states that is responsible for the high concentration of Tb^{3+} cations. This phenomenon illustrates how important can be metal $\leftrightarrow$ oxygen $\leftrightarrow$ metal interactions for determining the properties of a ternary oxide.

[1] *Catalysis by Ceria and Related Materials*, edited by A. Trovarelli (World Scientific, London, 2002).

[2] V. E. Henrich and P. A. Cox, *The Surface Science of Metal Oxides* (Cambridge University Press, Cambridge, UK, 1994).

[3] (a) A. F. Wells, *Structural Inorganic Chemistry*, 6th ed. (Oxford, New York, 1987); (b) M. Shelef and G. W. Graham, Catal. Rev. - Sci. Eng. **36**, 433 (1994); (c) *Application of Solid Electrolytes*, edited by T. Takahashi and A. Kozawa (JEC, Ohio, 1980); (d) H. Inaba and H. Tagawa, Solid State Ionics **83**, 1 (1996).

[4] R. W. Wyckoff, *Crystal Structures*, 2nd ed. (Wiley, New York, 1964).

[5] H. Nöremberg and G. A. D. Briggs, Phys. Rev. Lett. **79**, 4222 (1997).

[6] (a) A. Fujimori, Phys. Rev. B **28**, 2281 (1983); (b) E. Wuillioud, B. Delley, W.-D. Schneider, and Y. Baer, Phys. Rev. Lett. **53**, 202 (1984); (c) F. Marabelli and P. Wachter, Phys. Rev. B **36**, 1238 (1987).

[7] D. D. Koelling, A. M. Boring, and J. H. Wood, Solid State Commun. **47**, 227 (1983).

[8] X. Wang, J. C. Hanson, G. Liu, J. A. Rodriguez, A. Iglesias-Juez, and M. Fernández-García, J. Chem. Phys. **121**, 5434 (2004).

[9] (a) M. Fernández-García, A. Martínez-Arias, A. Guerrero-Ruiz, J. C. Conesa, and J. Soria, J. Catal. **211**, 326 (2002); (b) A. Iglesias-Juez, A. B. Hungría, O. Gálvez, A. Martínez-Arias, M. Fernández-García, J. C. Conesa, and J. Soria, Stud. Surf. Sci. Catal. **138**, 347 (2001); (c) M. Fernández-García, A. Martínez-Arias, A. B. Hungría, A. Iglesias-Juez, J. C. Conesa, and J. Soria, Phys. Chem. Chem. Phys. **4**, 2473 (2002); (d) A. B. Hungria, A. Martínez-Arias, M. Fernández-García, A. Iglesias-Juez, A. Guerrero-Ruiz, J. J. Calvino, J. C. Conesa, and J. Soria, Chem. Mater. **15**, 4309 (2003).

[10] (a) S. de Carolis, J. L. Pascual, L. G. M. Petterson, M. Baudin, M. Wojcik, K. Hermansson, A. E. C. Palmqvist, and M. Muhammed, J. Phys. Chem. B **103**, 7627 (1999); (b) G. Balducci, M. Islam, J. Kašpar, P. Fornasiero, and M. Graziani, Chem. Mater. **12**, 677 (2000); (c) W. Liu, C. Wadia, and M. Flytzani-Stephanopoulos, Catal. Today **28**, 391 (1996); (d) Q. Fu, H. Saltsburg, and M. Flytzani-Stephanopoulos, Science **301**, 935 (2003); (e) R. Si, Y.-W. Zhang, S.-J. Li, B.-X. Lin, and C.-H. Yan, J. Phys. Chem. B **108**, 12481 (2004).

[11] (a) S. Park, J. M. Vohs, and R. J. Gorte, Nature (London) **404**, 265 (2000); (b) Y. Nigara, W. Watanabe, J. Mizusaki, and M. Ishigame, J. Electrochem. Soc. **144**, 1050 (1997).

[12] W. A. Harrison, *Electronic Structure and the Properties of Solids* (Dover, New York, 1980).

[13] (a) M. T. Weller, *Inorganic Materials Chemistry* (Oxford, New York, 1994); (b) A. R. West, *Solid State Chemistry and Its Applications* (Wiley, New York, 1997).

[14] M. A. Peña and J. L. G. Fierro, Chem. Rev. (Washington, D.C.) **101**, 1981 (2001).

[15] J. A. Rodriguez, Theor. Chem. Acc. **107**, 117 (2002); Catal. Today **85**, 177 (2003).

[16] M. Fernández-García, A. Martínez-Arias, J. C. Hanson, and J. A. Rodriguez, Chem. Rev. (Washington, D.C.) **104**, 4063 (2004).

[17] J. A. Rodriguez, X. Wang, G. Liu, J. C. Hanson, J. Hrbek, C. H. F. Peden, A. Iglesias-Juez, and M. Fernández-García, J. Mol. Catal. A: Chem. **228**, 11 (2005).

[18] J. A. Rodriguez, J. C. Hanson, J.-Y. Kim, G. Liu, A. Iglesias-Juez, and M. Fernández-García, J. Phys. Chem. B **107**, 3535 (2003).

[19] J. A. Rodriguez, X. Wang, J. C. Hanson, G. Liu, A. Iglesias-Juez, and M. Fernández-García, J. Chem. Phys. **119**, 5659 (2003).

[20] M. Boaro, M. Vicario, C. de Leitenburg, G. Dolcetti, and A. Trovarelli, Catal. Today **77**, 407 (2003).

[21] S. Bernal, G. Blanco, M. A. Cauqui, M. P. Corchado, C. Larese, J. M. Pintado, and J. M. Rodriguez-Izquierdo, Catal. Today **53**, 607 (1999).

[22] (a) P. Norby and J. Hanson, Catal. Today **39**, 301 (1998), and references there in. (b) P. J. Chupas, M. F. Ciraolo, J. C. Hanson, and C. P. Grey, J. Am. Chem. Soc. **123**, 1694 (2001).

[23] A. P. Hammersely, S. O. Svensson, and A. Thompson, Nucl. Instrum. Methods Phys. Res. A **346**, 312 (1994).

[24] (a) A. C. Larson and R. B. von Dreele, *GSAS General Structure Analysis System*. Report LAUR 86-748, Los Alamos National Laboratory, Los Alamos, NM, 1995. (b) A. M. Reitveld, J. Appl. Crystallogr. **2**, 65 (1969).

[25] (a) REFLEX package provided by Accelrys; (b) P. Thompson, D. E. Cox,

and J. B. Hastings, J. Appl. Crystallogr. **20**, 79 (1987); (c) J. Baldinozzi and J. F. Berar, Nachr. Ges. Wiss. Goettingen, Math.-Phys. Kl. **26**, 128 (1993); (d) P. Scherrer, Nachr. Ges. Wiss. Goettingen, Math.-Phys. Kl. **2**, 98 (1918); (e) R. A. Young, *The Rietveld Method*, IUCR Mono. Cryst. Vol. 5 (Oxford, Oxford, 1993).

[26](a) V. Milman, B. Winkler, J. A. White, C. J. Pickard, M. C. Payne, E. V. Akhmatskaya, and R. H. Nobes, Int. J. Quantum Chem. **77**, 895 (2000); (b) M. C. Payne, D. C. Allan, T. A. Arias, and J. D. Johannopoulus, Rev. Mod. Phys. **64**, 1045 (1992).

[27](a) J. A. Rodriguez, Theor. Chem. Acc. **107**, 117 (2002); (b) I. Dawson, P. D. Bristowe, M. H. Lee, M. C. Payne, M. D. Segall, and J. M. White, Phys. Rev. B **54**, 13727 (1996); (c) P. J. D. Lindan, N. M. Harrison, J. M. Holender, and M. J. Gillan, Chem. Phys. Lett. **261**, 246 (1996).

[28]D. Vanderbilt, Phys. Rev. B **41**, 7892 (1990).

[29]H. J. Monkhorst and J. D. Pack, Phys. Rev. B **13**, 5188 (1976).

[30]J. P. Perdew, K. Burke, and M. Ernzerhof, Phys. Rev. Lett. **77**, 3865 (1996).

[31]J. A. Rodriguez, A. Etxeberria, L. González, and A. Maiti, J. Chem. Phys. **117**, 2699 (2002).

[32](a) M. D. Segall, C. J. Pickard, R. Shah, and M. C. Payne, Phys. Rev. B **54**, 16317 (1996); (b) D. Sánchez-Portal, E. Artacho, and J. M. Soler, J. Phys.: Condens. Matter **8**, 3859 (1996).

[33]K. B. Wiberg and P. R. Rablen, J. Comput. Chem. **14**, 1504 (1993); and references therein.

[34]D. M. Gruen, W. C. Koehler, and J. J. Katz, J. Am. Chem. Soc. **73**, 1475 (1951).

[35](a) A. Cox and M. J. L. Sangster, J. Phys. C **18**, L1123 (1985); (b) Z.-Z. Xu, J. Phys.: Condens. Matter **5**, 9077 (1993).

[36](a) M. Yashima, H. Arashi, M. Kakihana, and M. Yoshimura, J. Am. Ceram. Soc. **77**, 1067 (1994); (b) J. E. Spanier, R. D. Robinson, F. Zhang, S.-W. Chan, and J. P. Herman, Phys. Rev. B **64**, 245407 (2001).

[37](a) M. Fernández-García, Catal. Rev. - Sci. Eng. **44**, 59 (2002); (b) J. G. Chen, Surf. Sci. Rep. **30**, 1 (1997).

[38]A. Soldatov, T. S. Ivanchenko, S. D. Longa, A. Kotani, Y. Iwamoto, and A. Bianconi, Phys. Rev. B **50**, 5074 (1994).

[39]N. Thromat, C. Noguera, M. Gautier, F. Jollet, and J. P. Duraud, Phys. Rev. B **44**, 7904 (1991).

[40]Y. Nagai, T. Yamamoto, T. Tanaka, S. Yoshida, T. Nonaka, T. Okamoto, A. Suda, and M. Sugiura, Catal. Today **74**, 225 (2002).

[41]R. C. Karnatak, J. Alloys Compd. **192**, 64 (1993).

[42]P. Shuk, M. Greeblatt, and M. Croft, Chem. Mater. **11**, 473 (1999).

[43](a) G. Liu, J. A. Rodriguez, J. Hrbek, J. Dvorak, and C. H. F. Peden, J. Phys. Chem. B **105**, 7762 (2001); (b) G. Liu, J. A. Rodriguez, Z. Chang, J. Hrbek, and C. H. F. Peden, *ibid.* **108**, 2931 (2004); (c) S. H. Overbury and D. R. Mullins, *Catalysis by Ceria and Related Materials*, edited by A. Trovarelli (World Scientific, London, 2002), Chap. 9; (d) J. Stubenrauch and J. M. Vohs, J. Catal. **159**, 50 (1996); (e) R. M. Ferrizz, R. J. Gorte, and J. M. Vohs, Catal. Lett. **82**, 123 (2002).

[44](unpublished).

[45](a) S. Bernal, G. Blanco, M. A. Cauqui, M. P. Corchado, J. M. Pintado, and J. M. Rodriguez-Izquierdo, Chem. Commun. (Cambridge) **16**, 1545 (1997); (b) S. Bernal, G. Blanco, J. J. Delgado, J. M. Pintado, and J. M. Rodriguez-Izquierdo, J. Alloys Compd. **344**, 347 (2002); (c) Z. C. Kang and L. Eyring, *ibid.* **181**, 483 (1992).